THE JOURNAL OF PHYSICAL CHEMISTRY A
A JOURNAL OF THE AMERICAN CHEMICAL SOCIETY

pubs.acs.org/JPCA

Article

Boron Silicon $B_2Si_3^q$ and $B_3Si_2^p$ Clusters: The Smallest Aromatic Ribbons

Long Van Duong, Nguyen Ngoc Tri, Nguyen Phi Hung, and Minh Tho Nguyen*

Cite This: *J. Phys. Chem. A* 2022, 126, 3101−3109

Read Online

ACCESS | Metrics & More | Article Recommendations | Supporting Information

ABSTRACT: The small binary boron silicon clusters $B_2Si_3^q$ with q going from −2 to +2 and $B_3Si_2^p$ with p varying from −3 to +1 were reinvestigated using quantum chemical methods. The thermodynamic stability of these smallest ribbon structures is governed by both Hückel and ribbon models for aromaticity. The more negative the cluster charge, the more ribbon character is shown. In contrast, the more positive the charge state, the more pronounced the Hückel character becomes. The ribbon aromaticity character can also be classified into ribbon *aromatic, semiaromatic, antiaromatic, and triplet aromatic* when the electron configuration of a ribbon structure is described as $[...\pi^{2(n+1)}\sigma^{2n}]$, $[...\pi^{2n+1}\sigma^{2n}]$, $[...\pi^{2n}\sigma^{2n}]$, and $[...\pi^{2n+1}\sigma^{2n-1}]$, respectively. Geometry optimizations of the B_2Si_3 lowest-energy structure by some density functional theory (DFT) functionals result in a nonplanar shape because it possesses an antiaromatic ribbon character. However, its π aromaticity assigned by the Hückel rule is stronger in such a way that several other DFT and coupled-cluster theory CCSD(T) calculations show that B_2Si_3 is indeed stable in a planar form (C_s). A new global equilibrium structure for the anion $B_2Si_3^{2-}$, which is a ribbon semiaromatic species, was identified. Some benchmark tests were also carried out to evaluate the performance of popular methods for the treatment of binary B−Si clusters. At odds with some previous studies, we found that with reference to the high accuracy CCSD(T)/CBS method, the hybrid TPSSh functional is reliable for a structure search, whereas the hybrid B3LYP functional is more suitable for simulations of some experimental spectroscopic results.

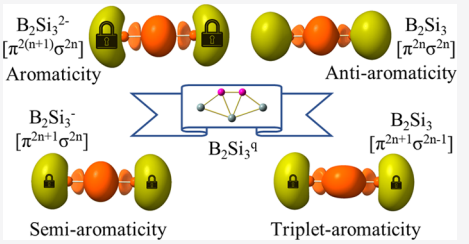

INTRODUCTION

The pure and doped boron clusters have been known to exist in a variety of geometrical shapes,[1−5] and thereby their structures can be accounted for by different models of chemical bonding. The aromaticity is, beyond any doubt, one of the most popular models of bonding for planar compounds. While the aromaticity of small-sized planar and quasiplanar structures of boron clusters[2,6−9] can effectively be rationalized by the classical Hückel rule, the larger planar and quasiplanar species having a circular shape do not obey the $4N + 2$ electron count but can be understood through the disk aromaticity model.[3,8,10,11] The double-ring (DR) motif was first found for the size B_{20},[12] while the smallest DR of pure boron cluster is the dication B_{14}^{2+}.[13] The hollow cylinder model[4,14] is proved to be more suitable for tubular structures such as the latter than the other models for cage-like structures, such as the Jellium model,[15] Clemenger−Nilsson model,[16,17] phenomenological shell model,[18] and so forth. Very recently, a new aromaticity model[19] has been proposed by some of us to explain the aromaticity character of the elongated boron structures.

Some double-chain or ribbon structures were previously found in boron clusters doped with different elements.[20−23] Although aromaticity models are diverse, their common characteristic is that aromaticity is a manifestation of electron delocalization in closed circuits, either in planar or three-dimensional structures.[24] This view poses a legitimate question as to whether a ribbon structure possesses a cyclic structure and then a corresponding aromaticity. Previous analyses[20] using the partial electron localization function[25] and nucleus-independent chemical shift (NICS)[26,27] methods elucidated the π and σ aromaticity alternations in magnetic properties of boron ribbon motifs. The ribbon aromaticity concept was proposed by Bai and co-workers[21] when investigating the stability of the series of $B_nH_2^{2-}$ and $Li_2B_nH_2$. This concept is based on the high thermodynamic stability of boron ribbons whose electronic configuration of $[...\pi^{2(n+1)}\sigma^{2n}]$ conforms to the classical Hückel counting rule ($4N + 2$). However, some of us[28] subsequently showed that the above result is purely coincidental and that the electronic configuration of $[...\pi^{2(n+1)}\sigma^{2n}]$ is only one part of a larger set of the π- and σ-aromaticity of the boron ribbon motif.[20] We then showed how ribbon aromaticity can appear in such a double chain structural motif, which is effectively a cyclic entity. The first consideration concerns the *self-lock* phenomenon that appears in a ribbon structure where the bond length of the two

Received: January 22, 2022
Revised: April 2, 2022
Published: May 12, 2022

https://doi.org/10.1021/acs.jpca.2c00540
J. Phys. Chem. A 2022, 126, 3101−3109

terminals of the structure becomes much shorter than usual. The longer the ribbon structure, the more obvious this phenomenon is. The atoms at the terminals are unusually close to each other, which then causes a certain interatomic Coulombic repulsion. The latter interaction leads to a significant barrier at the terminals of the structure whereby both sets of π and σ-delocalized electrons move freely following the simplest Schrödinger equation for a particle in a one-dimensional box. According to the model for a particle moving in a one-dimensional box, the methods of determining the aromaticity of the ribbon motif should be done in a different way, that is, by determining the lengths of the structure. Let us note that the NICS method has been applied to the ribbon B_nH_2 structures at their rhombus center along the structures[22] and along the middle lines of some highly stable $B_nC_2H_2$ ribbon clusters.[20] Our survey[28] also showed that in addition to a *ribbon aromaticity* corresponding to a $[...\pi^{2(n+1)}\sigma^{2n}]$ electronic configuration, the $[...\pi^{2n+1}\sigma^{2n-1}]$ electronic configuration also gives rise to a *ribbon triplet aromaticity*. Although it is inherently difficult to compare the aromaticity models to each other, it can be seen that a *ribbon triplet aromaticity* is somewhat weaker than a *ribbon aromaticity* because of its weaker influence on the thermodynamic stability.

With the aim to further elucidate the influence of ribbon aromaticity on the structural stability, we set out to reinvestigate the geometrical and electronic structures of a set of small binary boron and silicon clusters through the charge variation, namely $B_2Si_3^q$ with the charge q going from −2 to 2 and $B_3Si_2^p$ with the charge p going from −3 to 1. Such molecular systems that are actually the smallest ribbon structures are suitable objects for a deeper investigation on how the ribbon and classical Hückel models for aromaticity simultaneously influence the thermodynamic stability of the same structure.

COMPUTATIONAL METHODS

Initial geometries of the small binary boron and silicon clusters $B_2Si_3^q$ and $B_3Si_2^p$ with the charge q = −2, −1, 0, and 2 and p = −3, −2, −1, 0, and 1 are constructed independently by using a stochastic search algorithm[29] which was implemented by our group[30−33] along with a manual search in view of the rather small number of atoms involved. All guess geometries are optimized using the density functional TPSSh in conjunction with the 6-311+G(d) basis set. Subsequent harmonic vibrational frequency calculations are carried out to verify that optimized structures are true energy minima. Both hand-built and code-based construction methods converge to the same set of low-lying isomers after full geometry optimizations. To evaluate the reliability of the different density functional theory (DFT) functionals, a benchmark analysis is performed and will be presented in the discussion. Electronic structure theory calculations are performed employing Gaussian 16 program.[34] Energies of the geometric isomers produced by each of the DFT functionals employed are then evaluated by performing single-point electronic energy computations using the coupled-cluster theory (U)CCSD(T) up to the complete basis set limit (CBS). ORCA program package[35] is used to obtain the (U)CCSD(T)/CBS energy which is extrapolated from (U)-CCSD(T) total energies computed using the aug-cc-pVxZ basis sets with x = D, T, and Q.

The single-reference CC energies obtained are reliable with the T1 diagnostic values below 0.02 or 0.04 for closed- or open-shell system.[36] Some T1 diagnostic values of trianion $B_3Si_2^{3-}$ are higher so that the multiconfigurational perturbation theory computations based on a completely active space wave function CASSCF/CASPT2[37] have been carried out by ORCA program package.[35] The CASSCF(12,12) and CASSCF-(11,12) wavefunctions are first constructed for the species having an even and odd electron number, respectively.

The net atomic charge (NAC) and bond order for each cluster are carried out using a density partitioning method, the DDEC6 atomic population analysis.[38,39] Dgrid 5.0 package[40] is used to calculate the electron localization function (ELF).[25]

RESULTS AND DISCUSSION

Geometrical Structures. The global equilibrium structures and some lower-lying isomers of $B_2Si_3^q$ with the charge q varying from −2 to +2 and $B_3Si_2^p$ with the charge p going from −3 to +1 are presented in Figures 1 and 2, respectively. Relative energies between isomers given in the following sections are obtained from (U)CCSD(T)/CBS + ZPE computations, unless otherwise noted.

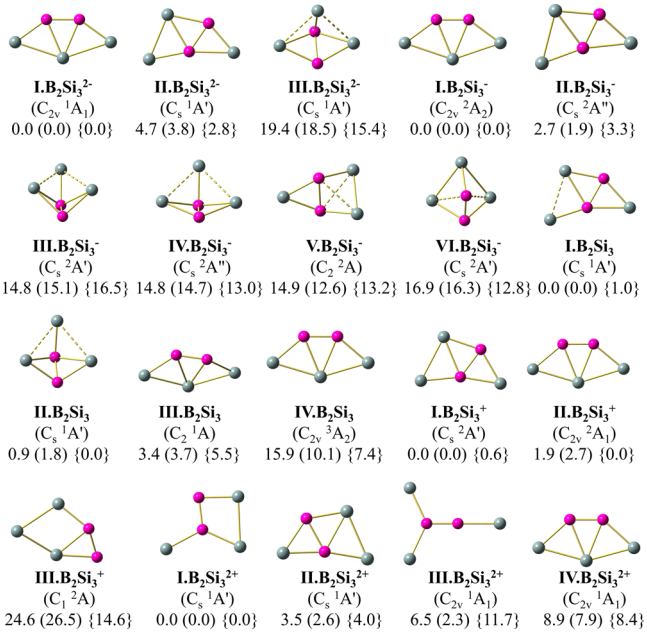

Figure 1. Shapes of low-lying isomers of $B_2Si_3^q$ clusters with q going from −2 to +2. Geometry optimizations are carried out using the TPSSh functional and 6-311+G(d) basis set. Relative energies are obtained by single point (U)CCSD(T)/CBS based on TPSSh/6-311+G(d)-geometries (TPSSh values given in parentheses), all with ZPE corrections [obtained by TPSSh/6-311+G(d) harmonic vibrational frequencies without scaling]. Relative energies obtained by single-point CASSCF/CASPT2 computation are given in brackets.

In order to further verify the identity of the ground states of the isomers considered, we carry out single-point multiconfigurational calculations using the complete active space CASSCF method with (n, 12) active spaces (n = 11 for doublet radicals, and n = 12 for both singlet and triplet structures), followed by second-perturbation theory CASPT2 calculations, with the TPSSh/6-311+G(d) optimized geometries and aug-cc-pVTZ basis set. The results are also added in Figures 1 and 2. The changes taking place in the series considered are small and do not modify the energy order. This is due to the fact that the wavefunctions of these structures are dominated by their Hartree−Fock references. As these isomers

https://doi.org/10.1021/acs.jpca.2c00540
J. Phys. Chem. A 2022, 126, 3101−3109

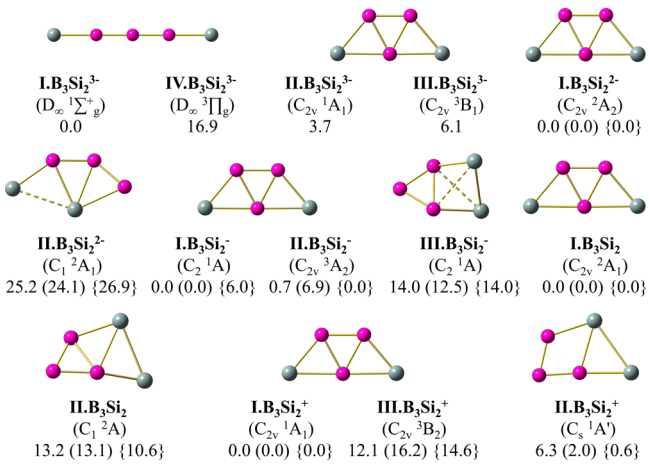

Figure 2. Shape of low-lying isomers of $B_3Si_2^p$ clusters with p in five charge states going from −3 to +1. Geometry optimizations are carried out using the TPSSh functional and 6-311+G(d) basis set. Relative energies are obtained by single-point (U)CCSD(T)/CBS and TPSSh/6-311+G(d) (values in parentheses), all with ZPE corrections [obtained by TPSSh/6-311+G(d) harmonic vibrational frequencies without scaling]. Relative energies obtained by single-point CASSCF/CASPT2 computations are given in brackets.

have basically single-reference electronic configurations, their relative energies obtained by the (U)CCSD(T) method are more reliable.

For the trianion $B_3Si_2^{3-}$, we could not get a proper CASSCF convergence for some isomers. Because the excess electrons tend to favor the MOs at higher energy levels distributed farther from the nuclei and are ready for electron detachment, it is a difficult task to determine accurately the ground state of this polyanion which requires much higher-level computation using a larger active space and a complete basis set to describe the excess electrons. In the present analysis, we simply consider this trianion as a model starting point for the formation of other species without a quantitative involvement of its energy.

The $B_2Si_3^{-/0}$ species were previously investigated by Lu *et al.*[41] using anion photoelectron spectroscopy and calculations. On the basis of the calculated CCSD results, Koukaras[42] subsequently concluded that the neutral B_2Si_3 is stable in a planar form, in contrast to previous results by calculations and experimental infrared spectroscopy reported by Truong and co-workers[43] that showed that it is slightly distorted from planarity.

Our first and foremost note is that the most stable anionic **I.$B_2Si_3^-$** structure (Figure 1) located in the present study was not found in the previous report by Lu and co-workers.[41] The anionic isomer **II.$B_2Si_3^-$**, which was assigned as the global minimum of $B_2Si_3^-$ by these authors,[41] is now found at 2.7 kcal/mol higher in energy than the new **I.$B_2Si_3^-$**, even though it remains competitive for the ground state in view of such a small energy difference. Such an omission by Lu *et al.*[41] could have been due to the fact that they used the B3LYP functional in their search for stable structures. Indeed, Koukaras[42] subsequently showed the erroneous performance of this hybrid functional on geometries of mixed boron clusters.

The latter author[42] performed a benchmarking test on several small binary B_nSi_m clusters with a diverse range of functionals in conjunction with the def2-QZVPP[44,45] basis set for negatively charged states and the def2-TZVP[44,45] for neutral or positively charged states. We find some inconvenience in using these basis sets when calculating the adiabatic and vertical detachment energies (ADEs and VDEs) of the anions, in which both neutral and anionic structures should be determined with a consistent method. In addition, the def2-QZVPP basis set is significantly more expensive than the def2-TZVP and some other basis sets we used.

Koukaras[42] also pointed out that the TPSSh/def2-TZVP level failed to produce the correct planar geometry for the neutral B_2Si_3 in such a way that the TPSSh functional is not classified as suitable for the mixed B−Si compounds. Our computed results disagree with this conclusion.

Figure 1 shows that TPSSh/6-311+G(d) calculations reproduce well the planar B_2Si_3 isomer **I.B_2Si_3** with a C_s point group, which is subsequently confirmed at CCSD(T) geometry optimizations and frequency analysis. Furthermore, the Pople-type 6-311+G(d) basis set,[46,47] which is more economic than the set of def2-TZVP, def2-QZVPP... basis sets, can uniformly be used for different charge states, thanks to the presence of a set of diffuse functions. In this context, we find it worthwhile to conduct another benchmarking test of density functionals and basis sets to ascertain the suitable level(s) for the treatment of the binary B−Si compounds.

Benchmarking Test for Stable Geometries. The global energy minimum structure of each charged state of the series

Table 1. Deviations of Single-Point CCSD(T)/CBS Total Energies of the Considered Structures Computed Using Geometries Optimized by Different DFT Levels[a]

optimized geometry	$B_3Si_2^{2-}$	$B_3Si_2^-$	B_3Si_2	$B_3Si_2^+$	$B_2Si_3^{2-}$	$B_2Si_3^-$	B_2Si_3	$B_2Si_3^+$	$B_2Si_3^{2+}$	RSM
B3LYP/6-311+G(d)	0.06	0.14	0.04	0.06	0.44	0.39	0.22	0.19	0.53	0.29
B3LYP/def2-QZVPP	0.14	0.21	0.12	0.14	0.21	0.20	0.15	0.14	0.44	0.22
PBE0/6-311+G(d)	0.02	0.01	0.03	0.07	0.02	0.02	0.00	0.03	0.15	0.06
PBE0/def2-QZVPP	0.11	0.09	0.11	0.17	0.17	0.09	0.05	0.09	0.13	0.12
HSE06/6-311+G(d)	0.02	0.00	0.03	0.07	0.02	0.01	0.00	0.03	0.13	0.05
HSE06/def2-QZVPP	0.11	0.08	0.11	0.17	0.14	0.07	0.04	0.09	0.11	0.11
TPSSh/6-311+G(d)	0.00	0.07	0.00	0.00	0.00	0.01	0.00	0.00	0.03	0.03
TPSSh/def2-QZVPP	0.02	0.10	0.02	0.05	0.05	0.01	0.61	0.02	0.00	0.21
TPSS-D3/6-311+G(d)	0.07	0.22	0.04	0.00	0.06	0.10	0.71	0.09	0.08	0.26
TPSS-D3/def2-QZVPP	0.01	0.19	0.01	0.01	0.00	0.00	1.24	0.04	0.00	0.42

[a]For each species, the values listed correspond to deviations of CCSD(T)/CBS energies at that DFT geometry with respect to the lowest CCSD(T)/CBS energy (obtained at a DFT level indicated by 0.00 kcal/mol). For each DFT level, the RMS of energy differences is given in the last column.

https://doi.org/10.1021/acs.jpca.2c00540
J. Phys. Chem. A 2022, 126, 3101−3109

Table 2. Comparison of Two PES Peaks of $B_2Si_3^-$ (Ref 41) to Calculated VDEs and ADEs (eV) Values Using Different Functionals with the 6-311+G(d) Basis Set and CCSD(T)/aug-cc-pVTZ for Both Anionic Isomers $I.B_2Si_3^-$ and $II.B_2Si_3^-$

isomer		B3LYP	PBE0	HSE06	TPSSh	TPSS-D3	CCSD(T)	Expt.[a]
$I.B_2Si_3^-$	VDE	2.63	2.80	2.78	2.78	2.76	2.63	2.64 ± 0.08
	ADE	2.60	2.76	2.75	2.74	2.71	2.61	
$II.B_2Si_3^-$	VDE	2.40	2.56	2.55	2.56	2.56	2.41	2.46 ± 0.08
	ADE	2.33	2.49	2.48	2.50	2.50	2.35	2.16 ± 0.08

[a]The VDEs and ADEs are taken from ref 41.

Table 3. Comparison of IR-UV2CI Spectra of B_2Si_3 (Ref 43) with Harmonic Vibrational Frequencies Calculated at the DFT/6-311+G(d) and CCSD(T)/aug-cc-pVTZ Levels

		υ_{calc} (cm^{-1})					
isomer	υ_{expt} (cm^{-1}) (ref 43)	B3LYP	PBE0	HSE06	TPSSh	TPSS-D3	CCSD(T)
$I.B_2Si_3$	491 (A)	500	517	515	497	470	498
	698 (B)	697	726	723	708	696	702

$B_2Si_3^q$ and $B_3Si_2^p$ (*cf.* Figures 1 and 2), except for the trianion $B_3S_2^{3-}$, are reoptimized employing DFT with several widely used functionals in conjunction with either the 6-311+G(d) or the def2-QZVPP basis set. The density functionals employed for these optimizations include the HSE06[48−50] and PBE0,[51] which are the two best functionals according to Koukaras' study,[42] B3LYP,[52,53] and TPSS-D3,[54] which have been used in studies where experimental results are available,[41,43] and the hybrid functional TPSSh.[55,56] Geometries produced by each DFT functional are evaluated by performing single-point electronic energy computations at these optimized geometries using the high-accuracy coupled-cluster CCSD(T)/CBS method. The CCSD(T)/CBS energy differences given in Table 1 are evaluated with respect to that of the lowest CC-energy isomer of each species for all the geometries obtained by the functionals under assessment. The root mean square (RMS), given in the last column of Table 1, can be used as a common index to probe the accuracy of optimized geometries. In spite of the fact that it is much less time-consuming to use than the def2-QZVPP basis set, the 6-311+G(d) counterpart consistently leads to significantly better results, as their RSM values are close to zero for the functional PBE0 or HSE06 or TPSSh. Thus, the functionals PBE0, HSE06, and TPSSh in conjunction with the 6-311+G(d) basis set are quite reliable approaches to investigate the geometries of stable mixed B−Si clusters in different charge states.

Benchmarking Test of Computations for Photoelectron Spectra. In their assignment of the experimental photoelectron (PE) spectrum of the anion $B_2Si_3^-$, Lu *et al.*[41] used the PBE0/aug-cc-PVDZ results as references to evaluate the values obtained by other functionals employed and concluded on a good performance of their B3LYP/6-311+G(d,p) results. Accordingly, the calculated VDE and ADE of the isomer $II.B_2Si_3^-$ (labeled as isomer **3A** in ref 41) amount to 2.46 and 2.16 eV by using both PBE0 and B3LYP functionals. However, our present computations using the PBE0/aug-cc-PVDZ point out that these VDE and ADE values are larger, being 2.57 and 2.50 eV, respectively. It is apparent that these authors misquoted their results because the values of 2.46 and 2.16 eV are actually the experimental PES data. In any case, they cannot be regarded as reference values as proposed in ref 41, simply because these authors failed to identify the lowest-lying isomer of the $B_2Si_3^-$ anion.

As stated above, our present structure $I.B_2Si_3^-$ is located to be the global energy minimum of the anion $B_2Si_3^-$ (*cf.* Figure 1). The VDE and ADE values for both isomers $I.B_2Si_3^-$ and $II.B_2Si_3^-$ determined using several density functionals and the 6-311+G(d) basis set along with the CCSD(T)/aug-cc-pVTZ level are presented in Table 2 and compared to available PES experimental results.[41] Surprisingly, in addition to the relevant CCSD(T) results, the B3LYP functional yields values much closer to experiment. This is not in line with the analysis reported by Koukaras in ref 42 and that mentioned above.

Our calculated results also allow us to offer a new assignment for the PE spectrum of the anion $B_2Si_3^-$. In fact, while the first PE peak having VDE = 2.46 eV and ADE = 2.16 eV are due to the isomer $II.B_2Si_3^-$, the peak identified with a VDE = 2.64 eV likely arises from the more stable isomer $I.B_2Si_3^-$. In other words, both anionic isomers, having an energy gap of ∼2−3 kcal/mol (Figure 1), are most probably present in the molecular beam of the PES experiment. The lowest-lying anionic isomer $I.B_2Si_3^-$ apparently generates a higher VDE peak.

Using the IR-UV2CI spectrometric techniques, Truong *et al.*[43] observed two clear vibrational bands peaking at 491 (A) and 698 (B) cm^{-1} and then assigned them to the coupled Si−B and B−B stretch modes. Harmonic vibrational frequencies of $I.B_2Si_3$ are carried out at both DFT/6-311+G(d) and CCSD(T)/aug-cc-pVTZ levels and listed in Table 3. These calculated vibrational modes confirm the above assignment. Again, both B3LYP and CCSD(T) levels provide us with the most consistent vibrational frequencies with respect to the experiment. For their part, TPSSh results can also be used to simulate vibrational spectra.

Ribbon Aromaticity Model *Versus* the Hückel Electron Count. We now turn to a rationalization for the stability of the remarkable structures displayed in Figures 1 and 2. The lowest-lying isomers of the trianion $B_3Si_2^{3-}$ include the global minimum, which belongs to the linear $I.B_3Si_2^{3-}$ and the second lower-lying isomer, which is a ribbon $II.B_3Si_2^{3-}$ structure[21−23,28] being 3.7 kcal/mol higher in relative energy. The doped boron ribbon motif is well-known with different elements as dopants, including H,[21,22,57] Li, and H,[21] C,[20] Si,[28] F,[23] or even Au,[57] and most of them exist in a negatively charged state. A boron ribbon motif is usually formed by two chains of B atoms having the same number of atoms in each chain (a D_{2h} motif) or with a difference of one atom between both chains (a C_{2v} motif). The dopants are often found to be located at both ends of the structure. The trianion $II.B_3Si_2^{3-}$ thus belongs to the C_{2v} motif. Figure 3 indicates that both

https://doi.org/10.1021/acs.jpca.2c00540
J. Phys. Chem. A 2022, 126, 3101−3109

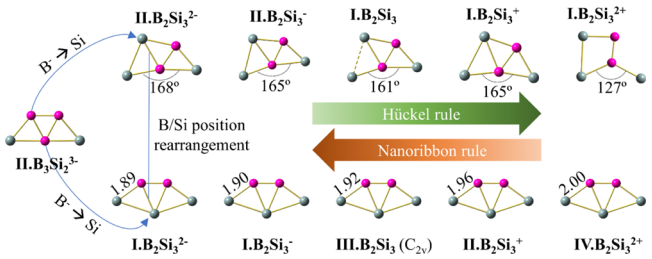

Figure 3. Pathway illustrating the evolution leading to the $B_2Si_3^{q}$ from the trianionic ribbon **II.B$_3$Si$_2$$^{3-}$** in which a B^- unit is replaced by an isovalent Si atom at two different positions leading to two isomeric types, namely ribbon (R) and Hückel (H).

isomers **I.B$_2$Si$_3$$^{2-}$** and **II.B$_2Si_3$$^{2-}$** are formed upon replacement of a B^- unit in **II.B$_3$Si$_2$$^{3-}$** at different positions by a Si atom. This can be done without significantly altering the electronic structure because each of both B^- and Si units contains four valence electrons. In keeping the total electron number, the ribbon rule of $[...\pi^{2(n+1)}\sigma^{2n}]$, which was established in previous studies,[21,23] can be applied.

Figure 4 shows that the structures **II.B$_3$Si$_2$$^{3-}$**, **I.B$_2Si_3$$^{2-}$**, and **II.B$_2Si_3$$^{2-}$** all satisfy this electron counting rule with $n = 1$

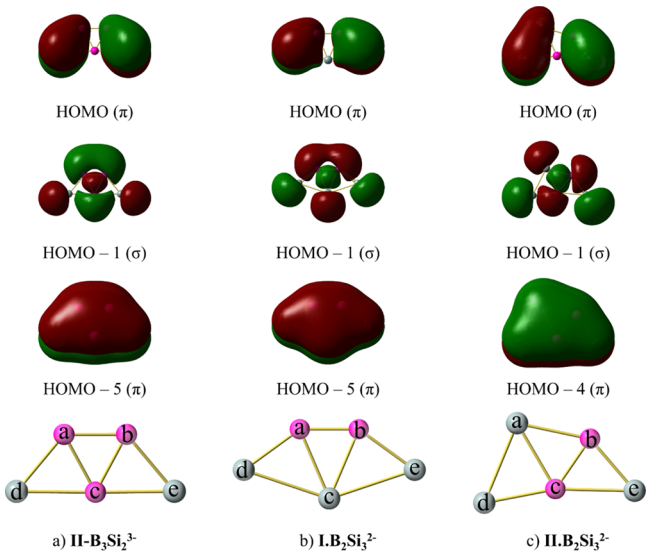

Figure 4. Delocalized π and delocalized σ CMOs of (a) **II.B$_3$Si$_2$$^{3-}$**, (b) **I.B$_2Si_3$$^{2-}$**, and (c) **II.B$_2Si_3$$^{2-}$** isomers. The atom positions are labeled by a, b, c, d, and e.

involving 4 π electrons and 2 σ-delocalized electrons. Accordingly, they are all considered *ribbon aromatic*. The bond lengths, bond orders,[38,39] NACs,[38,39] the ELF maps[40] at isosurface of ELF = 0.8, and the electronic configuration of the $B_3Si_2^{p}$ ribbon isomers with the charge p going from −3 to 1+ are shown in Figure 5. A *self-lock* phenomenon[28] is again observed in the model species **II.B$_3$Si$_2$$^{3-}$** following a shortening of the terminal B^a−Si^d and B^b−Si^e (*cf.* Figure 4 for atom labeling) bonds with bond lengths of ∼1.93 Å.

Lest us remind that a *self-lock* is a phenomenon in which the terminal bonds become significantly shortened. For ease of visualization, Figure S1 (Supporting Information file) presents a significant shortening of the B−B bonds at the terminal bonds as compared to those of the rest of the B−B bonds in the ribbon structures, including $B_7H_2^-$,[57] B_8H_2,[22] $B_9H_2^{3-}$, $B_9H_2Li_2^-$,[21] and $B_{10}H_2^{-}$[21] structures, in different charged

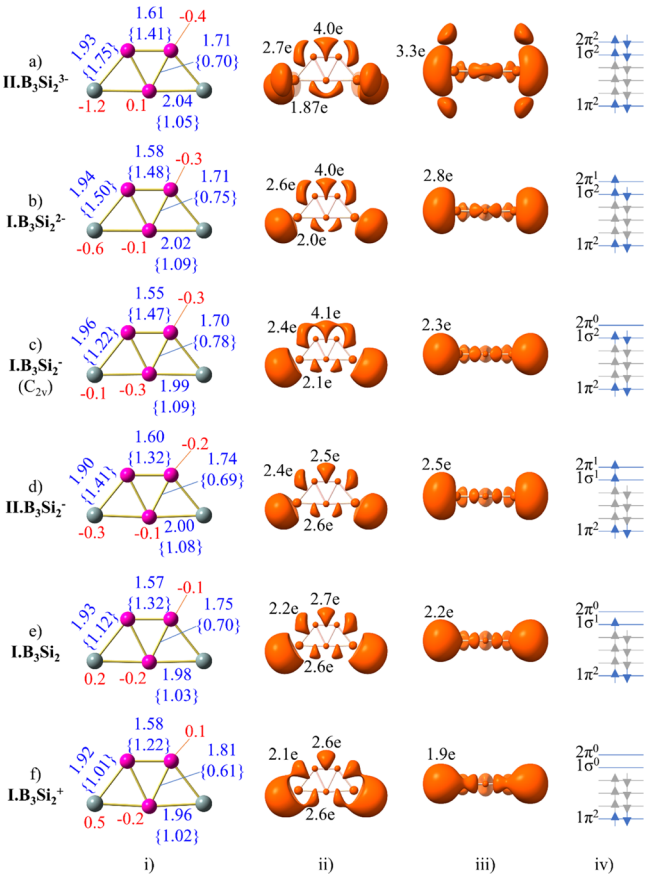

Figure 5. (a−d) Ribbon structures of $B_3Si_2^{p}$. (i) Bond lengths (Å) and bond orders (given in brackets) by blue numbers and NACs are given by red numbers. ELF isosurfaces of ELF = 0.8 under (ii) top view and (iii) side view. (iv) Electron configurations. Energy levels with green arrow(s) belong to π and σ-delocalized CMOs whereas energy levels with grey arrows point out localized CMOs.

states. Although in these systems, more electrons are added and the B−B length at the terminal bonds increases, a general picture is that the bond length at the terminal bonds is shorter than the remaining bonds. A self-lock phenomenon is hardly recognized in the trianion **II.B$_3$Si$_2$$^{3-}$** because of its small size and the redundancy of up to 3 electrons. The electron excess leads to an increase in the average bond length of the molecule and tends to decrease the dimensionality of the structure. The latter effect explains the significantly stronger stability of the 1D isomer **I.B$_3$Si$_2$$^{3-}$** than the 2D **II.B$_3Si_2$$^{3-}$** by DFT calculations and explains the negative frequencies observed in the ribbon form of the trianion $B_9H_2^{3-}$.

Such a charge effect is eliminated when two electrons are replaced by two Li atoms, forming an aromatic ribbon $B_9H_2Li_2^-$ structure[21] or the $B_3Si_2Li_2^-$ (*cf.* Figure S2). The ribbon $B_{12}Si_2^{2-}$[28] includes the B−Si terminal bond length of ∼1.89 Å and the remaining B−B bond length in a range of 1.59−1.74 Å. In general, these bonds have an increased length in the many electron-excess structures of **II.B$_3$Si$_2$$^{3-}$** with the B−Si terminal bonds amounting to 1.93 Å and the B−B bonds to 1.62 and 1.72 Å. A consequence of the *self-lock* phenomenon is that the Coulombic repulsion between the nuclei of the two atoms at the terminal bond of the ribbon significantly increases, which is expected to lead to a substantial increase in the potential energy barrier between the two terminals of the structure, facilitating a suitable movement of delocalized

https://doi.org/10.1021/acs.jpca.2c00540
J. Phys. Chem. A 2022, 126, 3101−3109

electrons in a potential well model.[58] In the ribbon model, the π electrons and σ-delocalized electrons are considered to be free to move in a one-dimensional box of the width L_π and L_σ, respectively. Results reported in ref 28 clearly indicate that these widths can be determined if at least two CMOs are occupied (two π occupied MOs are needed for determining L_π and two σ occupied MOs for L_σ). In the case of $\mathbf{II.B_3Si_2^{3-}}$, we can easily calculate the width of L_π as 3.93 Å, which is very close to the distance between two Si atoms (4.09 Å).

The *self-lock* phenomenon appears to increase the nuclear repulsion energy of the ribbon species, and thus the electrons need to have a special distribution to compensate for such a problem. Such a special distribution indicates a strong overlap of π CMOs at terminal bonds (*cf.* the ELF_π map of $\mathbf{II.B_3Si_2^{3-}}$ and $\mathbf{I.B_2Si_3^{2-}}$ in Figure S3), whereas the σ-delocalized electrons cause the B^a-B^b bond shortened to ∼1.61 Å. The loss of one π electron from the trianion $\mathbf{II.B_3Si_2^{3-}}$ leads to the dianion $\mathbf{I.B_3Si_2^{2-}}$ with slightly longer terminal B^a-Si^d and B^b-Si^e bonds (1.94 Å) and a shorter B−B bond (1.58 Å). The electron removed from $\mathbf{I.B_3Si_2^{2-}}$ can be either a remaining π electron on the SOMO, leading to $\mathbf{I.B_3Si_2^-}$ (C_{2v}) having an imaginary frequency, or an σ electron on the SOMO − 1 resulting in the triplet anion $\mathbf{II.B_3Si_2^-}$. In $\mathbf{I.B_3Si_2^-}$ (C_{2v}), the terminal B^a-Si^d and B^b-Si^e bond distances amount to ∼1.96 Å and the B^a-B^b bond to 1.55 Å. Comparable effects are thus observed upon the successive removal of π electrons in going from the trianion $\mathbf{II.B_3Si_2^{3-}}$ to the dianion $\mathbf{I.B_3Si_2^{2-}}$ and then the anion $\mathbf{I.B_3Si_2^-}$ (C_{2v}; *cf.* Figure 5). Overall, most of the species considered above follow a self-lock phenomenon concerning their terminal bonds.

In addition to the change in bond length, the change in the bond order is more obvious when different electrons are removed from a structure. The bond order of B^a-Si^d and B^b-Si^e bonds rapidly decreases from 1.75 to 1.50, then to 1.22 upon removal of 1 π electron from $\mathbf{II.B_3Si_2^{3-}}$ giving $\mathbf{I.B_3Si_2^{2-}}$ and then to $\mathbf{I.B_3Si_2^-}$, whereas removal of that electron induces no appreciable effect on the order of other bonds. From the ribbon model viewpoint,[21,22,28] the trianion $\mathbf{II.B_3Si_2^{3-}}$ is characterized as an aromatic structure because its electron configuration of 4 π electrons and 2 σ-delocalized electrons fully satisfies the electron shell of a ribbon, namely $[...\boldsymbol{\pi}^{2(n+1)}\boldsymbol{\sigma}^{2n}]$ with n = 1. The *self-lock* phenomenon, which ensures the working of the ribbon model, is represented by the bond order difference of B^a-Si^d and B^b-Si^e bonds with respect to the rest of the bonds present in the structure.

As $\mathbf{II.B_3Si_2^{3-}}$ is *ribbon aromatic*, $\mathbf{I.B_3Si_2^{2-}}$ can be considered as a *ribbon semiaromatic* structure where the *terminal locks* remain strong enough to keep both the π and σ-delocalized electrons moving in a similar way as in the model of a free particle moving in the one-dimensional ribbon.[28] The removal of a π electron also implies a reduction in the influence of the π electrons set and allows the effects of σ electrons to become more pronounced. The unusual shortness of the B^a-B^b bond (1.55 Å) in the anion $\mathbf{I.B_3Si_2^-}$ (C_{2v}), which is due to an enhancement from σ-delocalized electrons after the removal of two π electrons, causes a distortion to form the stable $\mathbf{I.B_3Si_2^-}$ structure with C_2 symmetry. Therefore, $\mathbf{I.B_3Si_2^-}$ (C_{2v}) is a *ribbon antiaromatic* species with the electron configuration of $[...\boldsymbol{\pi}^{2n}\boldsymbol{\sigma}^{2n}]$ involving 2 π electrons and 2 σ-delocalized electrons. In this way of classification of ribbon types, the triplet ribbon $B_{10}Si_2^{2-}$ structure[28] can be classified into a *ribbon triplet aromatic* class with an electronic configuration $[...\boldsymbol{\pi}^{2n+1}\boldsymbol{\sigma}^{2n-1}]$ involving 3 π electrons and 1 σ-delocalized electrons. In this context, the triplet isomer $\mathbf{II.B_3Si_2^-}$ is also *ribbon triplet aromatic*.

Calculated NACs of the atoms given in Figure 5 show that Si atoms lose more electrons than B atoms when removing electrons one by one from $B_3Si_2^p$. The strength of the *locks* in these ribbons can clearly be observed from the monosynaptic basin of the centers Si^d and Si^e in their ELF maps [*cf.* Figure 5(ii,iii)]. These monosynaptic basins possess their own lone pair electrons of Si atoms, the p_z electrons contribute to the π-MOs, and p_x and p_y electrons contribute to σ-MOs. The decreasing number of electrons in these basins is consistent with the gradually positive charges observed in Si atoms. Because the width of the $3p_z$ orbital in Si is much larger than that of the $2p_z$ orbital in B, the ELF_π maps (*cf.* Figure S3) from the 2 π-MO do not fully observe the $3p_z$ of Si. The ELF maps from the side view [*cf.* Figure 5(iii)] emphasize that the *z*-width extension of these basins decreases when the π electron is removed from $\mathbf{II.B_3Si_2^{3-}}$ to form $\mathbf{I.B_3Si_2^{2-}}$ and from $\mathbf{I.B_3Si_2^{2-}}$ to form $\mathbf{I.B_3Si_2^-}$ (C_{2v}). This corresponds to a gradual loosening of the terminal locks, and thus the ribbon aromaticity character changes from *aromatic* to *semiaromatic* and to *antiaromatic*. The *z*-width extension of these basins does not seem to change when a σ electron is removed from $\mathbf{I.B_3Si_2^{2-}}$ to form $\mathbf{II.B_3Si_2^-}$. Such terminal locks of $\mathbf{II.B_3Si_2^-}$ are strong enough to guarantee a ribbon triplet aromatic character.

Bond orders of the B^a-Si^d and B^b-Si^e bonds of the B_3Si_2 and $B_3Si_2^+$ ribbon structures that approach the value of 1 indicate that the *self-lock* phenomenon is no longer present in these structures. Indeed, the monosynaptic basins of Si centers are small, and their terminal locks become too weak in such a way that the ribbon model no longer applies to these species. $\mathbf{I.B_3Si_2^+}$ can then be considered as π aromatic, whereas $\mathbf{I.B_3Si_2}$ is both π and σ aromatic, all assigned by the Hückel model.

Although both $\mathbf{I.B_2Si_3^{2-}}$ and $\mathbf{II.B_2Si_3^{2-}}$ are ribbon aromatic species, the C_{2v} symmetry of $\mathbf{I.B_2Si_3^{2-}}$ suggests that it is closer to the ribbon model than the $\mathbf{II.B_2Si_3^{2-}}$. At the same time, the ELF map (Figures S4a(ii) and S5a(ii)) of $\mathbf{II.B_2Si_3^{2-}}$ shows that the three monosynaptic basins of three Si centers are distributed roughly in a circular pattern around the structure in such a way that the influence of the Hückel model on $\mathbf{II.B_2Si_3^{2-}}$ is more pronounced than in $\mathbf{I.B_2Si_3^{2-}}$. In possessing 2 σ and 4 π electrons, both $\mathbf{I.B_2Si_3^{2-}}$ and $\mathbf{II.B_2Si_3^{2-}}$ are considered as having, in the meantime, a σ aromaticity and a π antiaromaticity according to the classical Hückel rule. Thus, a geometry closer to the ribbon motif $\mathbf{I.B_2Si_3^{2-}}$ and a more circular geometry $\mathbf{II.B_2Si_3^{2-}}$ seem to lead to a higher aromaticity character for $\mathbf{I.B_2Si_3^{2-}}$ than $\mathbf{II.B_2Si_3^{2-}}$, and as a result, $\mathbf{I.B_2Si_3^{2-}}$ turns out to be more stable than its next isomer $\mathbf{II.B_2Si_3^{2-}}$ by ∼5 kcal/mol. To facilitate the competitive characterization for the stability of such isomers, the superscript R (ribbon) and H (Hückel) are added to the structures derived from $\mathbf{I.B_2Si_3^{2-}}$ and $\mathbf{II.B_2Si_3^{2-}}$, respectively (*cf.* Figure 3).

Figure 3 shows that the $\widehat{Si^dB^cSi^e}$ bond angle marginally decreases from 168 to 165° and then to 161° when an electron is successively removed from the dianion $^{H}\mathbf{II.B_2Si_3^{2-}}$ to the anion $^{H}\mathbf{II.B_2Si_3^-}$ and to the neutral $^{H}\mathbf{I.B_2Si_3}$. A small decrease of this bond angle corresponds to a larger transformation of the structure into a circular shape, implying that it could become different from a ribbon. This is evidenced by a reduction in the relative energy between $^{R}\mathbf{I.B_2Si_3^-}$ and $^{H}\mathbf{II.B_2Si_3^-}$ to only ∼2

https://doi.org/10.1021/acs.jpca.2c00540
J. Phys. Chem. A 2022, 126, 3101−3109

kcal/mol, and a reversed energy order in the neutral state, with ^{H}**I.B$_2$Si$_3$** being ∼4 kcal/mol more stable than ^{R}**III.B$_2$Si$_3$** (C_{2v}).

Let us note that in neutral isomers, either ^{R}**III.B$_2$Si$_3$** (C_{2v}) or ^{H}**I.B$_2$Si$_3$** has 2 π and 2 σ electrons, implying that it can be considered doubly aromatic according to the Hückel electron count. This is expected to give the planar structure a higher thermodynamic stability. CCSD(T)/aug-cc-pVTZ calculations verify it for ^{H}**I.B$_2$Si$_3$** by the lowest harmonic vibrational frequency of ∼100 cm^{-1}. For ^{R}**III.B$_2$Si$_3$** (C_{2v}), the influence of the ribbon antiaromaticity appears to be stronger than the Hückel aromaticity, and the C_{2v} ribbon motif becomes less stable. This structure has a small lowest harmonic vibrational frequency (60 cm^{-1}) at the CCSD(T)/aug-cc-pVTZ level, but it is distorted to a C_2 point group at the TPSSh/6-311+G(d) level.

Similar to the case of **I.B$_3$Si$_2$** and **I.B$_3$Si$_2^+$**, the terminal locks in ^{R}**II.B$_2$Si$_3^+$** and ^{R}**IV.B$_2$Si$_3^{2+}$** are too weak to keep electrons moving freely along the length of the structure, and as a consequence, the influence of the ribbon model is getting weaker. The influence of the Hückel model then increases in both ^{H}**I.B$_2$Si$_3^+$** and ^{H}**I.B$_2$Si$_3^{2+}$**. In particular, the bond angle $\widehat{Si^dB^cSi^e}$ in ^{H}**I.B$_2$Si$_3^{2+}$** is equal now to 127°, being the smallest H-type structure under consideration, that is, the most circular one. Thus, ^{H}**I.B$_2$Si$_3^{2+}$** can be considered π aromatic, and its thermodynamic stability becomes superior to that of ^{R}**IV.B$_2$Si$_3^{2+}$** (up to ∼9 kcal/mol). Table 4 summarizes the aromatic characters of the investigated species. Let us stress again that in contrast to hydrocarbons in which an aromatic isomer is substantially more stable than its next nonaromatic isomer, a typical characteristic of atomic clusters is that many lower-lying isomers of a certain size have a similar energy content and an aromatic character, implying even a small stabilization energy is often large enough to allow an aromatic isomer to emerge as the global energy minimum.

Table 4. Summary of the Aromaticity Characters of the Species Considered

electronic configuration	aromaticity character: R = ribbon, H = Hückel, S = strong, W = weak, Aro = aromatic		
$[\pi^4\sigma^2]$	**II.B$_3$Si$_2^{3-}$**	**I.B$_2$Si$_3^{2-}$**	**II.B$_2$Si$_3^{2-}$**
	R: ^{S}Aro	R: ^{S}Aro	R: ^{W}Aro
	H: none	H: $^{W}\pi$-anti; $^{W}\sigma$-aro	H: $^{S}\pi$-anti; $^{S}\sigma$-aro
$[\pi^3\sigma^2]$	**I.B$_3$Si$_2^{2-}$**	**I.B$_2$Si$_3^-$**	**II.B$_2$Si$_3^-$**
	R: ^{S}semi-aro	R: ^{S}semi-aro	R: ^{W}semi-aro
	H: none	H: $^{W}\pi$-anti; $^{W}\sigma$-aro	H: $^{S}\pi$-anti; $^{S}\sigma$-aro
$[\pi^2\sigma^2]$	**I.B$_3$Si$_2^-$** (C_{2v})	**III.B$_2$Si$_3$** (C_{2v})	**I.B$_2$Si$_3$**
	R: ^{W}anti-aro	R: ^{W}anti-aro	R: ^{W}anti-aro
	H: none	H: $^{W}\pi$-aro; $^{W}\sigma$-aro	H: $^{S}\pi$-aro; $^{S}\sigma$-aro
$[\pi^3\sigma^1]$	**II.B$_3$Si$_2^-$**	**IV.B$_2$Si$_3$**	
	R: ^{S}triplet-aro	R: ^{S}triplet-aro	
	H: none	H: $^{W}\pi$-anti; $^{W}\sigma$-aro	
$[\pi^2\sigma^1]$	**I.B$_3$Si$_2$**	**II.B$_2$Si$_3^+$**	**I.B$_2$Si$_3^+$**
	R: none	R: none	R: none
	H: $^{W}\pi$-aro; $^{W}\sigma$-aro	H: $^{W}\pi$-aro; $^{W}\sigma$-aro	H: $^{S}\pi$-aro; $^{S}\sigma$-aro
$[\pi^2\sigma^0]$	**I.B$_3$Si$_2^+$**	**IV.B$_2$Si$_3^{2+}$**	**I.B$_2$Si$_3^{2+}$**
	R: none	R: none	R: none
	H: $^{W}\pi$-aro	H: $^{W}\pi$-aro	H: $^{S}\pi$-aro

Finally, for verification of the reliability of the ribbon aromaticity model for these small structures, we perform substitution of a Si atom by a BH unit, both of which are isovalent, within a framework similar to an isolobal analogy[59,60] for $B_3Si_2^-$. The result of such an operation, shown in Figure 6,

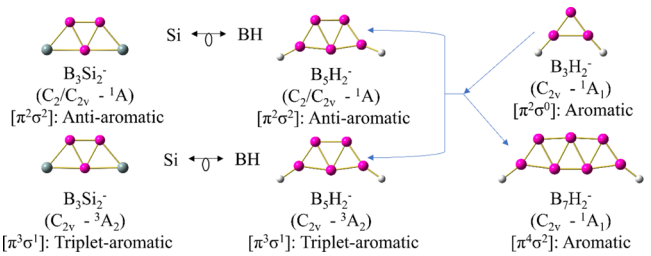

Figure 6. Analogy between $B_3Si_2^-$ and $B_5H_2^-$, and a prediction of two ribbon aromatic species, $B_3H_2^-$ and $B_7H_2^-$.

leads to a global energy minimum of $B_5H_2^-$, which is antiaromatic in the singlet state and aromatic in the triplet state. Furthermore, we would also predict that the borane hydride anions $B_{2m+1}H_2^-$ that are situated before and after the size $B_5H_2^-$ are equally ribbon aromatic structures. Indeed, the $B_3H_2^-$ anion is the smallest structure that is considered to have a ribbon aromaticity even though it can perfectly be considered as Hückel π-aromatic, whereas the $B_7H_2^-$ anion, given earlier by Zhai *et al.*,[57] has a ribbon aromaticity with a configuration of $[\pi^4\sigma^2]$. This consideration suggests that some correspondence between borane hydrides and boron−silicon clusters deserves to be more deeply analyzed in future studies.

CONCLUDING REMARKS

In this theoretical reinvestigation of the small binary boron silicon clusters, we identified a new global equilibrium structure **I.B$_2$Si$_3^-$** for the anion $B_2Si_3^-$, which was missing in a previous paper by Lu and co-workers.[41] The new and most stable isomer **I.B$_2$Si$_3^-$** is likely responsible for a higher energy peak observed in the experimental photoelectron spectrum of the anion. Its higher thermodynamic stability can be attributed to the semiaromaticity of its ribbon structure.

With respect to the performance of the current density functionals, the hybrid TPSSh functional appears reliable in the search for geometries and the determination of relative energy ordering of Si clusters (with a small number of B atoms), whereas the popular hybrid B3LYP functional can be used to simulate the experimental PE and IR spectra. The use of the 6-311+G(d) basis set seems sufficient for these spectroscopic assignments. In this context, the claims in previous papers for "good" assignments of experimental (PE and IR) spectra[41,43] of a small-size cluster that were achieved with an incomplete set of geometrical structures are concerning.

The ribbon aromaticity model is classified into *aromaticity*, *semiaromaticity*, *antiaromaticity*, and *triplet-aromaticity* types when the electronic configuration of $[...\pi^{2(n+1)}\sigma^{2n}]$, $[...\pi^{2n+1}\sigma^{2n}]$, $[...\pi^{2n}\sigma^{2n}]$, and $[...\pi^{2n+1}\sigma^{2n-1}]$ are involved, respectively. The isomers **II.B$_3$Si$_2^{3-}$**, **I.B$_2$Si$_3^{2-}$**, and **II.B$_2$Si$_3^{2-}$** are assigned as ribbon aromatic species, whereas the **I.B$_3$Si$_2^{2-}$**, **I.B$_2$Si$_3^-$**, and **II.B$_2$Si$_3^-$** are ribbon semiaromatic species. The ribbon antiaromatic character of **I.B$_3$Si$_2^-$** (C_{2v}) and **III.B$_2$Si$_3$** (C_{2v}) is assigned because it leads them to a distortion to a lower symmetry (C_2). Although the neutral **I.B$_2$Si$_3$** has a

https://doi.org/10.1021/acs.jpca.2c00540
J. Phys. Chem. A 2022, 126, 3101−3109

ribbon antiaromaticity, it has a more pronounced π aromatic nature according to the conventional Hückel rule. Because it is effectively influenced by both models going in opposite directions, one antiaromatic and one aromatic, the distortion of the **I.B_2Si_3** structure when optimized by several DFT functionals is understandable. In general, each small geometrical change due to an addition or a removal of an electron from both ribbon **R**- and Hückel **H**-type structures is also manifested in an increase or decrease in the degree of aromaticity corresponding to either the ribbon or the Hückel model.

■ ASSOCIATED CONTENT

Supporting Information

The Supporting Information is available free of charge at https://pubs.acs.org/doi/10.1021/acs.jpca.2c00540.

Shape of $B_7H_2^-$, B_8H_2, $B_9H_2^{3-}$, $B_9H_2Li_2^-$, $B_{10}H_2^-$, and $B_3Si_2Li_2^-$; ELF_π maps for **II.$B_3Si_2^{3-}$** and **I.$B_2Si_3^{2-}$**; and bonding properties of $B_2Si_3^q$ (PDF)

■ AUTHOR INFORMATION

Corresponding Author

Minh Tho Nguyen − *Institute for Computational Science and Technology (ICST), Ho Chi Minh City 700000, Vietnam;* orcid.org/0000-0002-3803-0569; Email: tho.nm@icst.org.vn, minh.nguyen@kuleuven.be

Authors

Long Van Duong − *Laboratory for Computational Molecular and Materials Sciences, Science and Technology Advanced Institute, Van Lang University, Ho Chi Minh City 700000, Vietnam; Faculty of Technology, Van Lang University, Ho Chi Minh City 700000, Vietnam*

Nguyen Ngoc Tri − *Department of Chemistry, Faculty of Natural Sciences, Quy Nhon University, Quy Nhon 55100, Vietnam*

Nguyen Phi Hung − *Department of Chemistry, Faculty of Natural Sciences, Quy Nhon University, Quy Nhon 55100, Vietnam*

Complete contact information is available at: https://pubs.acs.org/10.1021/acs.jpca.2c00540

Notes

The authors declare no competing financial interest.

■ ACKNOWLEDGMENTS

L.V.D. is grateful to Van Lang University. M.T.N. used the computing resources at the HPC Center of the Institute for Computational Science and Technology at Ho Chi Minh City (ICST). This research was funded by the Department of Science and Technology of Ho Chi Minh City, Vietnam, under the grant nos. 414/QĐ-KHCNTT and 1398/QĐ-SKHCN.

■ REFERENCES

(1) Tai, T. B.; Grant, D. J.; Nguyen, M. T.; Dixon, D. A. Thermochemistry and Electronic Structure of Small Boron Clusters (B_n , n = 5−13) and Their Anions. *J. Phys. Chem. A* **2010**, *114*, 994−1007.

(2) Tai, T. B.; Tam, N. M.; Nguyen, M. T. The Boron Conundrum: The Case of Cationic Clusters B_n^+ with n = 2-20. *Theor. Chem. Acc.* **2012**, *131*, 1241.

(3) Tai, T. B.; Duong, L. V.; Pham, H. T.; Mai, D. T. T.; Nguyen, M. T. A Disk-Aromatic Bowl Cluster B_{30} : Toward Formation of Boron Buckyballs. *Chem. Commun.* **2014**, *50*, 1558−1560.

(4) Duong, L. V.; Pham, H. T.; Tam, N. M.; Nguyen, M. T. A Particle on a Hollow Cylinder: The Triple Ring Tubular Cluster B_{27}^+. *Phys. Chem. Chem. Phys.* **2014**, *16*, 19470−19478.

(5) Barroso, J.; Pan, S.; Merino, G. Structural Transformations in Boron Clusters Induced by Metal Doping. *Chem. Soc. Rev.* **2022**, *51*, 1098−1123.

(6) Rincon, L.; Almeida, R.; Alvarellos, J. E.; Garcia-Aldea, D.; Hasmy, A.; Gonzalez, C. The σ Delocalization in Planar Boron Clusters. *J. Chem. Soc., Dalton Trans.* **2009**, *17*, 3328−3333.

(7) Cias, P.; Araki, M.; Denisov, A.; Maier, J. P. Gas Phase Detection of Cyclic B_3: 2^2 E′ ← X^2 A'_1 Electronic Origin Band. *J. Chem. Phys.* **2004**, *121*, 6776−6778.

(8) Pham, H. T.; Lim, K. Z.; Havenith, R. W. A.; Nguyen, M. T. Aromatic Character of Planar Boron-Based Clusters Revisited by Ring Current Calculations. *Phys. Chem. Chem. Phys.* **2016**, *18*, 11919−11931.

(9) Islas, R.; Inostroza, D.; Arias-Olivares, D.; Zúñiga-Gutiérrez, B.; Poater, J.; Solà, M. Analysis of the Electronic Delocalization in Some Isoelectronic Analogues of B_{12} doped with Beryllium and/or Carbon. *Phys. Chem. Chem. Phys.* **2020**, *22*, 12245−12259.

(10) Pham, H. T.; Duong, L. V.; Tam, N. M.; Pham-Ho, M. P.; Nguyen, M. T. The Boron Conundrum: Bonding in the Bowl B_{30} and B_{36}, Fullerene B_{40} and Triple Ring B_{42} Clusters. *Chem. Phys. Lett.* **2014**, *608*, 295−302.

(11) Tai, T. B.; Havenith, R. W. A.; Teunissen, J. L.; Dok, A. R.; Hallaert, S. D.; Nguyen, M. T.; Ceulemans, A. Particle on a Boron Disk: Ring Currents and Disk Aromaticity in B_{20}^{2-}. *Inorg. Chem.* **2013**, *52*, 10595−10600.

(12) Kiran, B.; Bulusu, S.; Zhai, H.-J.; Yoo, S.; Zeng, X. C.; Wang, L.-S. Planar-to-Tubular Structural Transition in Boron Clusters: B_{20} as the Embryo of Single-Walled Boron Nanotubes. *Proc. Natl. Acad. Sci. U.S.A.* **2005**, *102*, 961−964.

(13) Yuan, Y.; Cheng, L. B_{14}^{2+}: A Magic Number Double-Ring Cluster. *J. Chem. Phys.* **2012**, *137*, 044308.

(14) Pham, H. T.; Duong, L. V.; Nguyen, M. T. Electronic Structure and Chemical Bonding in the Double Ring Tubular Boron Clusters. *J. Phys. Chem. C* **2014**, *118*, 24181−24187.

(15) Ekardt, W. Work Function of Small Metal Particles: Self-Consistent Spherical Jellium-Background Model. *Phys. Rev. B: Condens. Matter Mater. Phys.* **1984**, *29*, 1558−1564.

(16) Knight, W. D.; Clemenger, K.; De Heer, W. A.; Saunders, W. A.; Chou, M. Y.; Cohen, M. L. Electronic Shell Structure and Abundances of Sodium Clusters. *Phys. Rev. Lett.* **1984**, *52*, 2141−2143.

(17) Nilsson, S. G. K. Dan. Vidensk. *Selsk., Mat.-Fys. Medd.* **1955**, *29*, 431.

(18) Chattaraj, P. K.; Höltzl, T. Phenomenological Shell Model and Aromaticity in Metal Clusters. *Aromaticity and Metal Clusters*; CRC Press, 2018; pp 281−306.

(19) Duong, L. V.; Mai, D. T. T.; Pham-Ho, M. P.; Nguyen, M. T. A Theoretical Approach to the Role of Different Types of Electrons in Planar Elongated Boron Clusters. *Phys. Chem. Chem. Phys.* **2019**, *21*, 13030−13039.

(20) Zhang, S.-Y.; Bai, H.; Chen, Q.; Mu, Y.-W.; Gao, T.; Lu, H.; Li, S.-D. Ribbon Aromaticity of Double-Chain $B_{2n}C_2H_2$ Clusters (n = 2−9): A First Principle Study. *J. Cluster Sci.* **2015**, *26*, 2043−2050.

(21) Bai, H.; Chen, Q.; Miao, C.-Q.; Mu, Y.-W.; Wu, Y.-B.; Lu, H.-G.; Zhai, H.-J.; Li, S.-D. Ribbon Aromaticity in Double-Chain Planar $B_nH_2^{2-}$ and $Li_2B_nH_2$ nanoribbon Clusters up to n = 22: Lithiated Boron Dihydride Analogues of Polyenes. *Phys. Chem. Chem. Phys.* **2013**, *15*, 18872−18880.

(22) Li, D.-Z.; Chen, Q.; Wu, Y.-B.; Lu, H.-G.; Li, S.-D. Double-Chain Planar D_{2h} B_4H_2, C_{2h} B_8H_2, and C_{2h} $B_{12}H_2$: Conjugated Aromatic Borenes. *Phys. Chem. Chem. Phys.* **2012**, *14*, 14769−14778.

(23) Bai, H.; Bai, B.; Zhang, L.; Huang, W.; Zhai, H.-J.; Li, S.-D. $B_{12}F_n^{0/-}$ (n = 1-6) Series: When Do Boron Double Chain

Nanoribbons Become Global Minima? *Phys. Chem. Chem. Phys.* **2017**, *19*, 31655−31665.
(24) Chen, Z.; Wannere, C. S.; Corminboeuf, C.; Puchta, R.; Schleyer, P. v. R. NICS as an Aromaticity Criterion. *Chem. Rev.* **2005**, *105*, 3842.
(25) Savin, A.; Nesper, R.; Wengert, S.; Fässler, T. F. ELF: The Electron Localization Function. *Angew. Chem., Int. Ed.* **1997**, *36*, 1808−1832.
(26) Schleyer, P. V. R.; Maerker, C.; Dransfeld, A.; Jiao, H.; Van Eikema Hommes, N. J. R. Nucleus-Independent Chemical Shifts: A Simple and Efficient Aromaticity Probe. *J. Am. Chem. Soc.* **1996**, *118*, 6317−6318.
(27) Schleyer, P. v. R.; Jiao, H.; Hommes, N. J. R. v. E.; Malkin, V. G.; Malkina, O. L. An Evaluation of the Aromaticity of Inorganic Rings: Refined Evidence from Magnetic Properties. *J. Am. Chem. Soc.* **1997**, *119*, 12669−12670.
(28) Van Duong, L.; Tho Nguyen, M. Silicon Doped Boron Clusters: How to Make Stable Ribbons? *Phys. Chem. Chem. Phys.* **2017**, *19*, 14913−14918.
(29) Saunders, M. Stochastic Search for Isomers on a Quantum Mechanical Surface. *J. Comput. Chem.* **2004**, *25*, 621−626.
(30) Pham, H. T.; Duong, L. V.; Pham, B. Q.; Nguyen, M. T. The 2D-to-3D Geometry Hopping in Small Boron Clusters: The Charge Effect. *Chem. Phys. Lett.* **2013**, *577*, 32−37.
(31) Mai, D. T. T.; Duong, L. V.; Tai, T. B.; Nguyen, M. T. Electronic Structure and Thermochemical Parameters of the Silicon-Doped Boron Clusters B_nSi, with n = 8-14, and Their Anions. *J. Phys. Chem. A* **2016**, *120*, 3623−3633.
(32) Van Duong, L.; Nguyen, M. T. Electronic Structure of the Boron Fullerene B_{14} and Its Silicon Derivatives $B_{13}Si^+$, $B_{13}Si^-$ and $B_{12}Si_2$: A Rationalization Using a Cylinder Model. *Phys. Chem. Chem. Phys.* **2016**, *18*, 17619−17626.
(33) Tam, N. M.; Duong, L. V.; Cuong, N. T.; Nguyen, M. T. Structure, Stability, Absorption Spectra and Aromaticity of the Singly and Doubly Silicon Doped Aluminum Clusters $Al_nSi_m^{0/+}$ with n = 3−16 and m = 1, 2. *RSC Adv.* **2019**, *9*, 27208−27223.
(34) Frisch, M. J.; Trucks, G. W.; Schlegel, H. B.; Scuseria, G. E.; Robb, M. A.; Cheeseman, J. R.; Scalmani, G.; Barone, V.; Petersson, G. A.; Nakatsuji, H.; et al. *Gaussian 16*, Revision C.01; Gaussian, Inc.: Wallingford, CT, 2019.
(35) Neese, F. Software Update: The ORCA Program System, Version 4.0. *Wiley Interdiscip. Rev.: Comput. Mol. Sci.* **2018**, *8*, No. e1327.
(36) Rienstra-Kiracofe, J. C.; Allen, W. D.; Schaefer, H. F. $C_2H_5+O_2$ Reaction Mechanism: High-Level Ab Initio Characterizations. *J. Phys. Chem. A* **2000**, *104*, 9823−9840.
(37) Andersson, K.; Malmqvist, P. Å.; Roos, B. O. Second-order Perturbation Theory with a Complete Active Space Self-consistent Field Reference Function. *J. Chem. Phys.* **1992**, *96*, 1218−1226.
(38) Manz, T. A.; Limas, N. G. Introducing DDEC6 Atomic Population Analysis: Part 1. Charge Partitioning Theory and Methodology. *RSC Adv.* **2016**, *6*, 47771−47801.
(39) Manz, T. A. Introducing DDEC6 Atomic Population Analysis: Part 3. Comprehensive Method to Compute Bond Orders. *RSC Adv.* **2017**, *7*, 45552−45581.
(40) Kohout, M. *DGrid*, Version 5.0; Springer: Dresden, 2017.
(41) Lu, S.-J.; Xu, X.-L.; Cao, G.-J.; Xu, H.-G.; Zheng, W.-J. Structural Evolution of $B_2Si_n^{-/0}$ (n = 3-12) Clusters: Size-Selected Anion Photoelectron Spectroscopy and Theoretical Calculations. *J. Phys. Chem. C* **2018**, *122*, 2391−2401.
(42) Koukaras, E. N. Ab Initio Study of Medium Sized Boron-Doped Silicon Clusters Si_nB_m, n = 11-13, m = 1-3. *Phys. Chem. Chem. Phys.* **2018**, *20*, 18556−18570.
(43) Truong, N. X.; Jaeger, B. K. A.; Gewinner, S.; Schöllkopf, W.; Fielicke, A.; Dopfer, O. Infrared Spectroscopy and Structures of Boron-Doped Silicon Clusters (Si_nB_m, n = 3-8, m = 1-2). *J. Phys. Chem. C* **2017**, *121*, 9560−9571.
(44) Weigend, F.; Ahlrichs, R. Balanced Basis Sets of Split Valence, Triple Zeta Valence and Quadruple Zeta Valence Quality for H to Rn: Design and Assessment of Accuracy. *Phys. Chem. Chem. Phys.* **2005**, *7*, 3297−3308.
(45) Weigend, F. Accurate Coulomb-Fitting Basis Sets for H to Rn. *Phys. Chem. Chem. Phys.* **2006**, *8*, 1057−1067.
(46) Krishnan, R.; Binkley, J. S.; Seeger, R.; Pople, J. A. Self-Consistent Molecular Orbital Methods. XX. A Basis Set for Correlated Wave Functions. *J. Chem. Phys.* **1980**, *72*, 650−654.
(47) Clark, T.; Chandrasekhar, J.; Spitznagel, G. n. W.; Schleyer, P. V. R. Efficient Diffuse Function-augmented Basis Sets for Anion Calculations. III. The 3-21+G Basis Set for First-row Elements, Li−F. *J. Comput. Chem.* **1983**, *4*, 294−301.
(48) Paier, J.; Marsman, M.; Hummer, K.; Kresse, G.; Gerber, I. C.; Ángyán, J. G. Screened Hybrid Density Functionals Applied to Solids. *J. Chem. Phys.* **2006**, *124*, 154709.
(49) Paier, J.; Marsman, M.; Hummer, K.; Kresse, G.; Gerber, I. C.; Ángyán, J. G. Erratum: Screened Hybrid Density Functionals Applied to Solids. [J. Chem. Phys. 2006, 124, 154709 (2006)]. *J. Chem. Phys.* **2006**, *125*, 249901.
(50) Krukau, A. V.; Vydrov, O. A.; Izmaylov, A. F.; Scuseria, G. E. Influence of the Exchange Screening Parameter on the Performance of Screened Hybrid Functionals. *J. Chem. Phys.* **2006**, *125*, 224106.
(51) Adamo, C.; Barone, V. Toward Reliable Density Functional Methods without Adjustable Parameters: The PBE0 Model. *J. Chem. Phys.* **1999**, *110*, 6158−6170.
(52) Becke, A. D. Density-functional Thermochemistry. III. The Role of Exact Exchange. *J. Chem. Phys.* **1993**, *98*, 5648−5652.
(53) Lee, C.; Yang, W.; Parr, R. G. Development of the Colle-Salvetti Correlation-Energy Formula into a Functional of the Electron Density. *Phys. Rev. B: Condens. Matter Mater. Phys.* **1988**, *37*, 785−789.
(54) Chai, J.-D.; Head-Gordon, M. Systematic Optimization of Long-Range Corrected Hybrid Density Functionals. *J. Chem. Phys.* **2008**, *128*, 084106.
(55) Tao, J.; Perdew, J. P.; Staroverov, V. N.; Scuseria, G. E. Climbing the Density Functional Ladder: Nonempirical Meta−Generalized Gradient Approximation Designed for Molecules and Solids. *Phys. Rev. Lett.* **2003**, *91*, 146401.
(56) Staroverov, V. N.; Scuseria, G. E.; Tao, J.; Perdew, J. P. Comparative Assessment of a New Nonempirical Density Functional: Molecules and Hydrogen-Bonded Complexes. *J. Chem. Phys.* **2003**, *119*, 12129−12137.
(57) Zhai, H.-J.; Wang, L.-S.; Zubarev, D. Y.; Boldyrev, A. I. Gold Apes Hydrogen. the Structure and Bonding in the Planar B_7Au_2 and B_7Au_2 Clusters. *J. Phys. Chem. A* **2006**, *110*, 1689−1693.
(58) Steiner, E. *The Chemistry Maths Book*; Oxford University Press: Oxford, 2008.
(59) Zdetsis, A. D. Success and Pitfalls of the $Si_{n-2}C_2H_2−C_2B_{n-2}H_n$ Isolobal Analogy: Depth and Breadth of the Boron Connection. *J. Chem. Phys.* **2009**, *130*, 064303.
(60) Zdetsis, A. D. Designing Novel Sn-Bi, Si-C and Ge-C Nanostructures, Using Simple Theoretical Chemical Similarities. *Nanoscale Res. Lett.* **2011**, *6*, 362.

https://doi.org/10.1021/acs.jpca.2c00540
J. Phys. Chem. A 2022, 126, 3101−3109